HYDRO ELASTIC BEHAVIOR OF VIBRATING BLADES

AUTHORS

C. Münch, P. Ausoni, O. Braun, M. Farhat, F. Avellan

Laboratory for Hydraulic Machines, EPFL, Lausanne, Switzerland

Tel: +41 (21) 693-3643; Fax: +41 (21) 693-3554

cecile.munch@epfl.ch

philippe.ausoni@epfl.ch

olivier.braun@epfl.ch

mohamed.farhat@epfl.ch

francois.avellan@epfl.ch

ABSTRACT

Fluid-structure investigations in hydraulic machines using coupled simulations are extremely time-consuming; therefore we develop an alternative method. In this paper, a model is proposed to predict fluid-structure coupling by linearizing the hydrodynamic load acting on a rigid oscillating 2D hydrofoil surrounded by an incompressible turbulent flow. Forced and free pitching motions are considered with a mean incidence of 0° and maximum amplitude of 2°. Unsteady flow simulations, performed with ANSYS CFX, are presented and validated with experiments carried out in the EPFL High-Speed Cavitation Tunnel. The hydrodynamic moment is assumed to result from three actions: inertia, damping and stiffness. The forced motion is investigated for reduced frequencies ranging from 0.02 to 100. As expected by the potential flow analysis, the added moment of inertia is found constant, while the fluid damping and the fluid stiffness coefficients are found to depend solely on the reduced frequency after an appropriate scaling. Behavioral patterns are observed and two different cases are identified depending on the development of vortices in the hydrofoil wake. Using the coefficients identified in the forced motion case, the time history of the profile incidence is then predicted analytically in the free motion case. An excellent agreement is observed with results from coupled fluid-structure simulations. The model is validated and can then be extended to more complex cases such as blade assemblies.

KEY WORDS: Fluid-structure, hydrofoil, added mass, fluid damping, fluid stiffness.

INTRODUCTION

Fluid structure interactions play a significant role in many engineering applications and particularly in turbo machinery. For instance, rotor-stator interaction induces pressure fluctuations which can lead to vibrations of the guide vane or resonance in the distributor channels, see Zobeiri (2006) [1] and Nicolet (2006) [2]. Flow-induced vibrations of the guide vane excited by the von Karman vortices can also lead to premature cracks, see Ausoni (2007) [3]. The elastic behavior of vibrating blade assemblies is thus of strong interest to design reliable and resistant turbines. The actual predictive methods to model fluid-structure coupling for aero engines or gas turbines are divided into two classes, see Marshall (1996) [4]: classical and integrated, depending on the coupling strength. The former combines the fluid and structural equations in an uncoupled way, whereas the latter solves the equations simultaneously.

Coupled simulations of the hydraulic machines with classical or integrated method are extremely time-consuming for complex geometries therefore we develop an alternative method. The unsteady incompressible turbulent flow around an oscillating rigid 2D hydrofoil is numerically and experimentally investigated. The hydrodynamic moment is assumed to result from three actions: inertia, damping and stiffness. The determination of the inertial effect has been largely investigated. Formulae have been established to estimate added mass and added moment of inertia for simple geometries, see Brennen (1982) [5]. Empirical formulae are not available for the fluid damping and the fluid stiffness effects. Experiments and numerical simulations are required to identify those effects depending on the surrounding flow and the structure motion. The forced motion case is first investigated in the frequency domain to identify the three coefficients. The free motion case is then used to assess the model.

After a description of the case study, as well as the numerical and experimental set up, the results are presented. The numerical simulations are validated: the grid and time step independencies are checked and a good agreement is observed by comparing the fluid torque with experiments. The hydrodynamic load is then analyzed. The method to determine the added moment of inertia, the fluid damping and fluid stiffness coefficient is detailed and assessed. Finally concluding remarks are made.

SET UP

Cases study

The investigated hydrofoil is a blunt trailing edge NACA 0009, see Abbott (1945) [6], having 100mm length with a maximum thickness of 9.27mm, see Figure 1. Forced and free oscillations of the hydrofoil are considered, see Figure 1. In both cases, the hydrofoil rotates around its center of mass with a mean incidence $\alpha_c = 0°$ and amplitude $\alpha_o = 2°$.
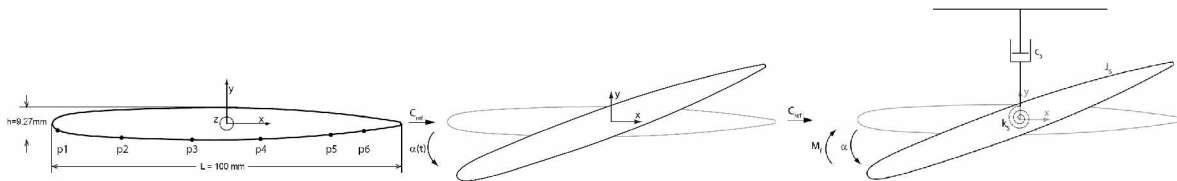

Figure 1 2D NACA 0009 Hydrofoil, Sketches of forced oscillating case and free oscillating case.

For the forced oscillating case, the incidence angle is defined by equation (1), with angular pulsation ω imposed.

$$\alpha(t) = \alpha_c + \alpha_o \sin(\omega t) \qquad (1)$$

The conditions investigated are summarized in Table 1. We note the upstream velocity C_{ref}, the reduced frequency $\kappa = \omega L/2C_{ref}$ and the Reynolds number $\text{Re} = C_{ref}L/\nu$.

Table 1 Forced motion : numerical and experimental conditions

Case	α_o	C_{ref}	Frequency	κ	Re
Numerical	2°	$5,10,15 \text{ m}\cdot\text{s}^{-1}$	$1-1000 \text{ Hz}$	$0.02-100$	$0.5-1.5\ 10^6$
Experimental			$2,10,20 \text{ Hz}$	$0.04-1.25$	$0.5-1.5\ 10^6$

For the free motion case, the hydrofoil is attached to a flexible structure. This case consists of a 1-degree-of-freedom model of an oscillating hydrofoil. The structural parameters of the hydrofoil are the moment of inertia J_s, the stiffness k_s and the damping coefficient μ_s. The hydrofoil is departing at rest from the incidence angle α_o. A Fortran program has been implemented in the fluid solver to couple the structure motion with the fluid action. The new incidence of the hydrofoil is computed as a function of the structural parameters, the fluid torque M and the incidences at the previous time steps see equation 2.

$$\alpha^{n+1} = \alpha^n \left(2 - \frac{\mu_s}{J_s}\Delta t - \frac{k_s}{J_s}\Delta t^2 \right) + \alpha^{n-1}\left(\frac{\mu_s}{J_s}\Delta t - 1 \right) + \frac{\Delta t^2}{J_s}M^n \tag{2}$$

The conditions for the numerical simulations are given in Table 2.

Table 2 Free motion : conditions for the numerical simulations

α_o	C_{ref}	J_s	μ_s	k_s	Re
2°	$5 \text{ m}\cdot\text{s}^{-1}$	$1.\ 10^{-5} \text{ kg}\cdot\text{m}^2$	$4.\ 10^{-4} - 0.12 \text{ kg}\cdot\text{m}^2\cdot\text{s}^{-1}$	$1,\ 30 \text{ N}\cdot\text{m}$	$0.5\ 10^6$

Experimental procedure

The EPFL High-Speed Cavitation Tunnel, described on the left of Figure 2, is a closed loop with a test section of $150\times150\times750 \text{ mm}$, see Avellan (1987) [7]. The experimental 2D hydrofoil has a span B of 150 mm. An oscillating system is used to generate hydrofoil angular pitching oscillations for different values of frequency and amplitude. The driving system is detailed in Caron (2000) [8]. The operating conditions investigated are given in Table 1. Six miniature piezo-resistive pressure transducers are flush mounted along the chord length in one side of the hydrofoil; see Figure 1. These sensors have a diameter of 3 mm, a height of 1 mm and the measurement range is 0-7 bars. They are directly embedded in small chambers previously drilled inside the profile. Each chamber is connected to the surface through a small pipe filled with plastic compound, which also acts as a protective layer for the sensing element. This ensures a good surface finish and enables the fitting of pressure sensors in areas of the profile as thin as 2 mm without alteration of the hydraulic profile. The data acquisition system has 16 bits A/D resolution, a memory depth of 1 MSamples/channel and maximum sampling frequency of 51.2 KHz/channel. The pressure at the inlet of the test section is held constant and sufficiently high to avoid any cavitation development.

Numerical procedure

The unsteady numerical simulations are carried out with ANSYS CFX 11. This software, based on finite volume methods, solves the incompressible Unsteady Reynolds Averaged Navier-Stokes U.R.A.N.S equations in their conservative form and the mass conservation equation. The set of

24th Symposium on Hydraulic Machinery and Systems

equations is closed with a two-equation turbulence model: the Shear Stress Transport (SST), see Menter (1994) [9]. The backward Euler implicit scheme (second order in time) and an advection scheme (second order in space) are used. The hydrofoil is placed in a rectangular computation domain measuring $250 \times 150 \times 1\,mm$, discretized with a structured mesh of 40,000 nodes, see Figure 2. The motion of the hydrofoil wall is specified or calculated, depending on the forced and free motion cases and the deformable mesh is following the hydrofoil motion. The boundary conditions consist of a no-slip condition on the hydrofoil wall and symmetrical conditions on the top and bottom wall of the domain. Uniform velocity C_{ref} along $\ddot{x}$ direction is fixed at the inlet and a constant average static pressure is imposed at the outlet.
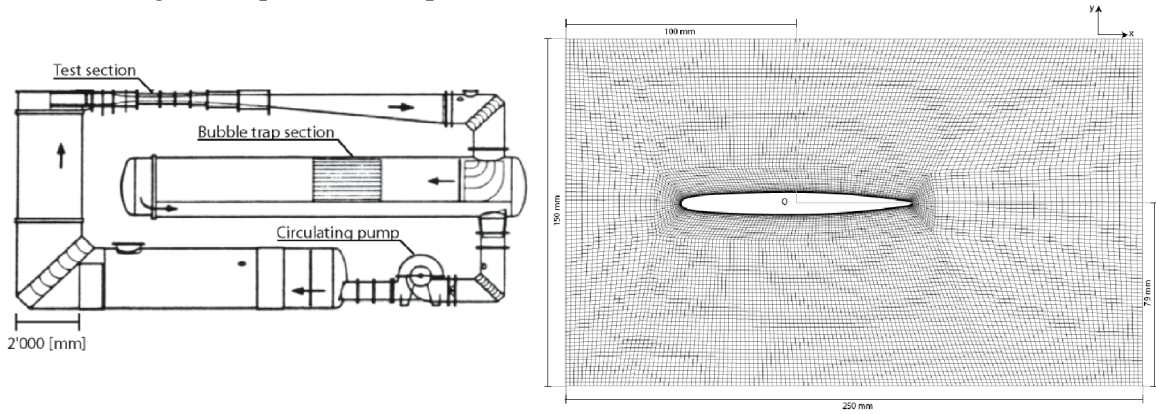

Figure 2 EPFL High Speed Cavitation Tunnel (Left), Computational domain (Right)

RESULTS

Experimental Validation

In this section, the numerical simulations are validated for the forced motion case. The fluid torque amplitude, M, is considered to check the mesh and time step independency. Three meshes are investigated, see Table 3. The difference between the medium and the fine mesh is smaller than 0.3%. The medium mesh is selected to save computational time. Three time steps are used: namely 120, 480 and 1920 iterations per period. The fluid torque amplitude with Δt_2 is only 0.25% higher that the case with the smaller time step. Each period will be discretized with 480 iterations to save computational time.

Table 3 Conditions of time step and mesh independency checks for $f=100Hz$ and $C_{ref}=10m.s^{-1}$

Case	Coarse	Medium	Fine	Δt_1	Δt_2	Δt_3
elements	20'000	40'000	80'000	40'000	40'000	40'000
Max y_{plus}	50	5	1	5	5	5
It.per period	480	480	480	120	480	1920
M_{max} [N.m]	$5.32\ 10^{-2}$	$5.38\ 10^{-2}$	$5.40\ 10^{-2}$	$5.44\ 10^{-2}$	$5.38\ 10^{-2}$	$5.37\ 10^{-2}$
Sensitivity	1.39 %	0.27 %	0 %	1.27 %	0.25 %	0 %

The numerical results are then validated by comparing the pressure coefficient with phase averaged experimental results; see Figure 3 on the left. The comparison shows an excellent agreement for the sensor location p_2 defined in Figure 1. The fluid torque is then calculated from the pressure at the

different sensor locations in both experimental and numerical cases. According to these comparisons, the numerical simulations correctly predict the pressure and thus the fluid torque.
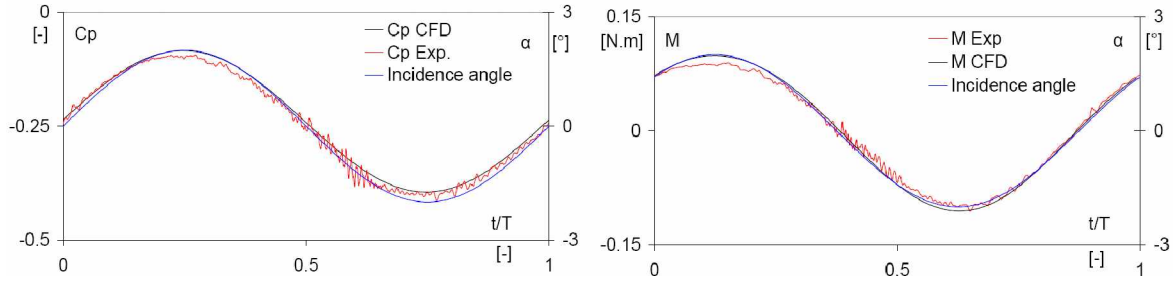

Figure 3 Experimental and numerical pressure coefficient at p_2 and fluid torque during one period for $\kappa = 0.21$

Fluid Torque: Numerical results and model

The model of the fluid torque is developed by assuming that the flow response is a linear function of the angular position and its derivatives see equation (3). The hydrodynamic moment is then assumed to result from three distinct actions: inertia, damping and stiffness.

$$M(t) = -\left(J_f \ddot{\alpha}(t) + \mu_f \dot{\alpha}(t) + k_f \alpha(t) \right) \tag{3}$$

The aim of the following analysis is to identify the three parameters of this model: the added moment of inertia J_f, the fluid damping coefficient μ_f and the fluid stiffness coefficient k_f. The forced motion is investigated to identify those coefficients.

Using the complex forms $\alpha(t) = \alpha_o e^{i\omega t}$, and $M(t) = M_o e^{i\omega t}$, equation (3) can be written as:

$$M_o = \alpha_o \left(J_f \omega^2 - k_f - i\mu_f \omega \right) \tag{4}$$

with α_o the motion amplitude and $M_o = M_{max} e^{-i\phi}$ the complex number taking into account the phase shift between the excitation and the system answer. The transfer function $H(\omega)$ describing the system is then introduced, see equation (5).

$$H(\omega) = \frac{\alpha_o}{M_o}$$

$$H(\omega) = \frac{1}{J_f \omega^2 - k_f - i\mu_f \omega} \tag{5}$$

The magnitude $\underline{H}(\omega)$ and the phase ϕ of the transfer function are both investigated in the frequency domain. A normalized form of the magnitude $\underline{H}^*$, see equation (6), is plotted as a function of the reduced frequency in Figure 4.

$$\underline{H}^*(\omega) = \frac{\underline{H}(\omega)}{\underline{H}_{C_{ref}=15}(0)} \times \left(\frac{C_{ref}}{15} \right)^2 \tag{6}$$

An excellent agreement is observed between the numerical and experimental results for the magnitude, which confirms the validity of the numerical simulation. At low frequencies, $\underline{H}^*$ tends to a constant value. For high frequencies, an asymptotic behavior is noticed. It corroborates the linear model, see equations (7) and (8).

$$\underline{H}(0) = \frac{1}{k_f} \tag{7}$$

$$\lim_{\omega \to \infty} \underline{H}(\omega) = \frac{1}{J_f \omega^2} \tag{8}$$
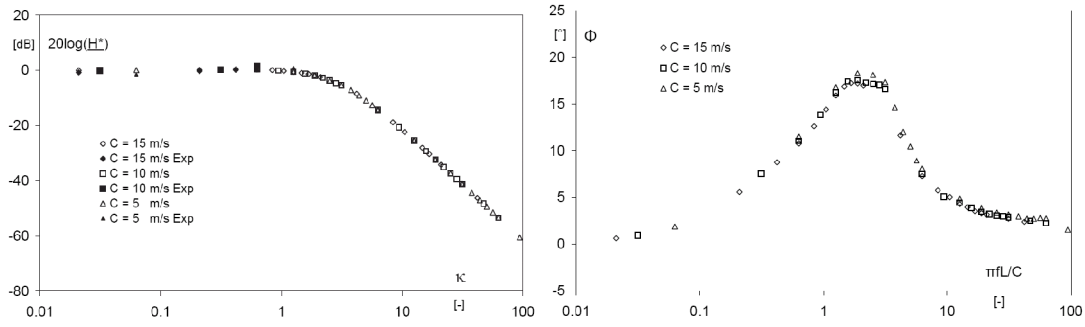

Figure 4 Normalized magnitude and phase of the transfer function for three values of the upstream velocity: numerical and experimental results.

In Figure 4 right, the phase shift between the forced motion and the fluid response is plotted as a function of the reduced frequency for three values of the upstream velocity. The phase shift is found to be independent of the upstream velocity in this range of Reynolds number values. A maximum value of $20°$ is reached for $\kappa \approx 1$, which corresponds to a transit-time and motion period of the same order. For $\kappa \quad 1$ and $\kappa \quad 1$, the hydrofoil motion and the torque are in phase ; the phase shift tends to the constant value of $0°$.

The added moment of inertia, the fluid damping and fluid stiffness coefficients are then identified. J_f is identified with the asymptotic matching of the magnitude for $\kappa \quad 1$, see equation (8). The estimated values for the three values of C_{ref} are given in Table 4. A comparison with the potential flow analysis is done, see Brennen (1982) [5] and equation (9).

$$J_B = \frac{1}{8} \rho \pi \left(\frac{L}{2}\right)^4 B \tag{9}$$

with B, the span and L, the chord. The added moment of inertia found with this formula is equal to the one computed in the three numerical simulations, see Table 4, which validates the assumption.

Table 4 Estimation of the added moment of inertia

C_{ref} $\left[\text{m}\cdot\text{s}^{-1}\right]$	5	10	15	Potential flow
J_f $\left[\text{kg}\cdot\text{m}^2\right]$	$2.46 \ 10^{-6}$	$2.45 \ 10^{-6}$	$2.45 \ 10^{-6}$	$2.45 \ 10^{-6}$

The fluid stiffness coefficient is identified with the real part of the transfer function:

$$k_f \left(\omega, C_{ref}\right) = J_f \omega^2 - \frac{\cos(\phi)}{\underline{H}} \tag{10}$$

A scaling of this coefficient is introduced. The dimensionless stiffness coefficient is defined by equation (11).

$$k^* = \frac{k_f}{\frac{1}{2} \rho C_{ref}^2 AL} \times \kappa \tag{11}$$

with C_{ref} the upstream velocity, L the chord and $A = L \times e$, a section. In Figure 5, k^* is plotted as a function of κ for three values of the upstream velocity as well as fitted quadratic laws. The right of the figure provides a focus on low frequency.
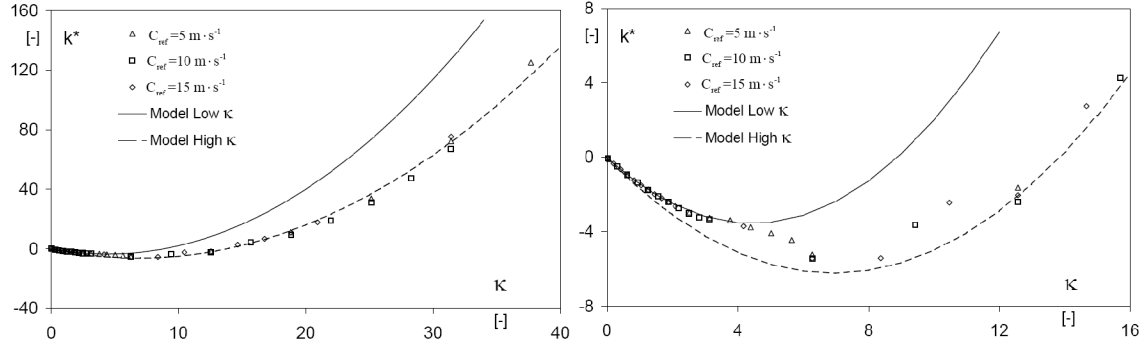

Figure 5 Dimensionless fluid stiffness coefficient as a function of the reduced frequency.

According to those results, k^* is found to be independent of the upstream velocity but strongly dependant on the reduced frequency. For $\kappa \leq 14$, the fluid stiffness tends to move the profile away from the reference position $\alpha = 0°$, k^* is negative. For $\kappa \leq 4$ and $\kappa \geq 12$, two quadratic behavioral laws are identified, see equations (12) and (13), represented in Figure 5 in solid and dashed lines respectively.

$$\kappa \leq 4, \quad k^* = 0.18\kappa^2 - 1.6\kappa \tag{12}$$

$$\kappa \geq 12, \quad k^* = 0.13\kappa^2 - 1.8\kappa \tag{13}$$

In between, a transitional behavior is observed. The origin of this transition will be illustrated later in the paper.

The fluid damping is then identified through the imaginary part of the transfer function.

$$\mu_f \left(\omega, C_{ref} \right) = \frac{\sin(\phi)}{\underline{H}\omega} \tag{14}$$

As for the fluid stiffness, the fluid damping is scaled following equation (15).

$$\mu^* = \frac{\mu_f}{\frac{1}{4}\rho C_{ref} AL^2} \times \kappa \tag{15}$$

In Figure 6, μ^* is plotted as a function of the reduced frequency for three values of the upstream velocity. The low values of κ are emphasized in Figure 6, right. As observed for k^*, μ^* is independent of the upstream velocity but varies with κ. This coefficient is always positive. For $\kappa \leq 4$ and $\kappa \geq 12$, two behavioral power laws are identified, see equations (16) and (17), represented in Figure 6 in solid and dashed lines respectively.

$$\kappa \leq 4, \quad \mu^* = 0.42\kappa^{0.6} \tag{16}$$

$$\kappa \geq 12, \quad \mu^* = 0.04\kappa^{1.6} \tag{17}$$

In between, as observed for k^*, a transitional behavior is observed for $4 \leq \kappa \leq 12$.
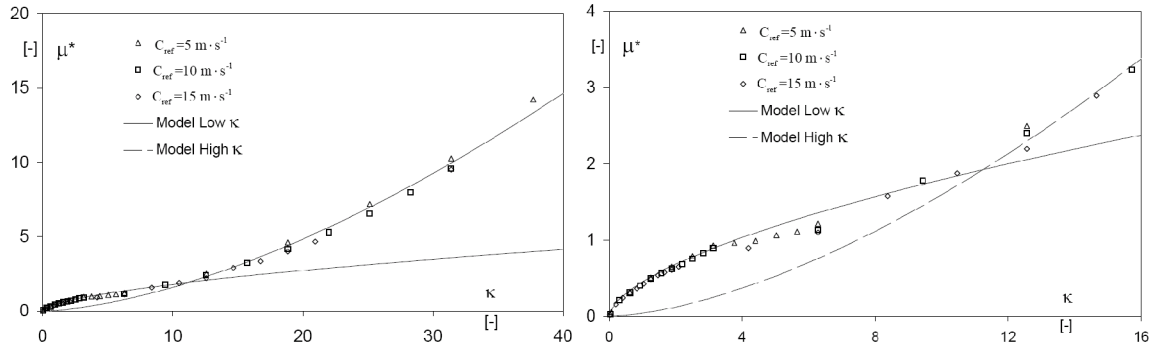
Figure 6 Dimensionless fluid damping coefficient as a function of the reduced frequency.

The flow dynamic around the hydrofoil is then investigated to identify the origin of the transition observed for μ^* and k^* for $4 \leq \kappa \leq 12$. In Figure 7, the scaled vorticity, defined by equation (18), is plotted for the case $C_{ref} = 15 \text{ m} \cdot \text{s}^{-1}$ for four values of the reduced frequency.

$$\Omega_n = \left(\frac{\partial C_y}{\partial x} - \frac{\partial C_x}{\partial y} \right) \frac{L}{C_{ref}} \tag{18}$$
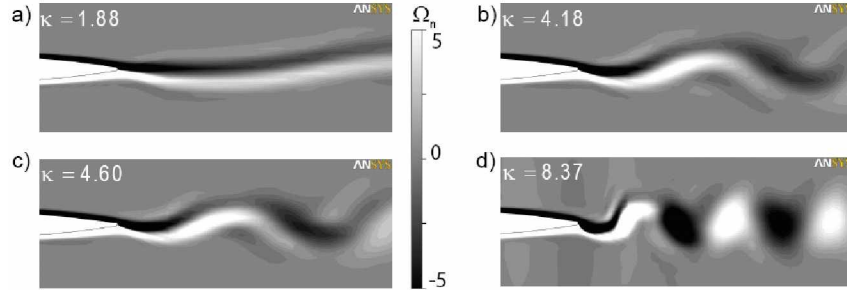

Figure 7 Cross sections of the scaled vorticity for four values of κ.

According to the four pictures in Figure 7, the flow dynamic in the wake starts to change dramatically for a reduced frequency equal to 4. The two layers of vorticity undulate with a decreasing wake length and cross from $\kappa \approx 4.6$. Then vortices develop, see Figure 7 d), as observed by Koochesfahani (1989) [10]. The development of those vortices has an influence on the fluid torque which explains the behavioral modification observed for k^* and μ^* for $4 \leq \kappa \leq 12$.

Model assessment

An assessment of the model is then made by considering the free motion of the hydrofoil. The free oscillating system is solution of equation (19).

$$M = J_s \ddot{\alpha} + \mu_s \dot{\alpha} + k_s \alpha \tag{19}$$

Using the linearized model for the fluid torque, the equation can be written as:

$$J_f \ddot{\alpha} + \mu_f \dot{\alpha} + k_f \alpha = J_s \ddot{\alpha} + \mu_s \dot{\alpha} + k_s \alpha \tag{20}$$

The damping ratio ξ and pulsation ω_o are introduced:

$$\xi = \frac{\mu_s + \mu_f}{2\sqrt{(k_s + k_f)(J_s + J_f)}} \tag{21}$$

$$\omega_o = \sqrt{\frac{k_s + k_f}{J_s + J_f}} \tag{22}$$

The equation to solve is then:

$$\ddot{\alpha} + 2\xi\omega_o\dot{\alpha} + \omega_o^2\alpha = 0 \tag{23}$$

The analytical solution in the under-damped case, $\xi < 1$, is:

$$\alpha = \alpha_o e^{-\xi\omega_o t}\left(\cos\left(\omega_o t\sqrt{1-\xi^2}\right) + \frac{\xi}{\sqrt{1-\xi^2}}\sin\left(\omega_o t\sqrt{1-\xi^2}\right)\right) \tag{24}$$

Two under-damped cases with different structural properties are considered, see Table 5. Two corresponding values of the reduced frequency are investigated to consider cases with and without development of vortices in the wake of the hydrofoil.

Table 5 Conditions of free motion for $C_{ref} = 5$ m.s^{-1} and results for model and simulations

	J_s	k_s	μ_s	κ	ξ^m	ξ^s	$\dfrac{\left|\xi^m - \xi^s\right|}{\xi^s}$	ω^m	ω^s	$\dfrac{\left|\omega^m - \omega^s\right|}{\omega^s}$
	$\left[\text{kg}\cdot\text{m}^2\right]$	$\left[\text{N}\cdot\text{m}\right]$	$\left[\text{kg}\cdot\text{m}^2\cdot\text{s}^{-1}\right]$	$[-]$	$[-]$	$[-]$	$[-]$	$\left[\text{rad}\cdot\text{s}^{-1}\right]$		$[-]$
a)	1.10^{-5}	1	4.10^{-4}	2.63	0.12	0.7 %	263	264	0.4 %
b)	1.10^{-5}	30	5.10^{-3}	15.5	0.14	1.4 %	1553	1560	0.4 %

A comparison of the damping ratios and frequencies computed with the model, $\left(\xi^m, \omega_o^m\right)$, and with the coupled fluid-structure simulation, $\left(\xi^s, \omega_o^s\right)$, are provided to assess the model. J_f, k_f, μ_f must be known to compute $\left(\xi^m, \omega_o^m\right)$. J_f is a constant, see Table 4, k_f and μ_f are calculated with the equations (12), (16) in case a) and (13), (17) in case b). $\left(\xi^s, \omega_o^s\right)$ are extracted by fitting the time history of the simulated value $\alpha(t)$ with equation (24). The results are given in Table 5. In both cases, the predicted values of $\left(\xi, \omega_o\right)$ with the model are very close to those obtained with the coupled numerical simulations. The difference for the frequencies is less than 0.5% and the damping values are predicted with an error less than 1.5%. To illustrate those results, the time history of the incidence angle in case a) and b) is plotted in Figure 8. An excellent agreement is actually observed. This proves that the simulation of the forced motion is sufficient to predict fluid-structure coupling in the free motion case, avoiding coupled fluid-structure simulations.
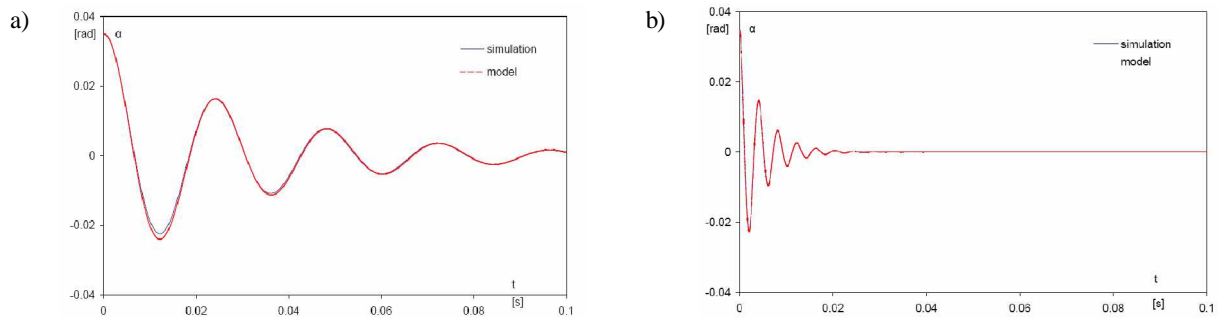

Figure 8 Results from the model and the simulations $\alpha(t)$ in cases a) and b).

CONCLUSIONS

Considering an oscillating NACA 0009 profile, this paper proposes a model to predict fluid-structure coupling by linearizing the hydrodynamic load acting on a rigid oscillating hydrofoil surrounded by an incompressible turbulent flow. Forced and free pitching motions are considered with a mean incidence of 0° and maximum amplitude of 2°. Unsteady simulations of the forced motion are carried out with ANSYS CFX and validated with corresponding experimental results. An analysis of the hydrodynamic load is then performed as a function of the reduced frequency, varying from 0.02 to 100. The added moment of inertia is found to be a constant as expected by the potential flow analysis. Behavior laws are identified for the fluid damping and fluid stiffness coefficients. The free motion is considered to validate the method. $\alpha(t)$ is first determined using the linearized model and then carried out with a coupled fluid-structure simulation. An excellent agreement is observed, as the differences for the damping ratio and the motion pulsation are less than 2 %. Those results show that this model can be used to predict fluid-structure interactions when linearized response of the system can be assumed.

ACKNOWLEDGEMENTS

REFERENCES

[1] ZOBEIRI, A., KUENY, J.-L., FAHRAT, M., AND AVELLAN, F. *Pump-Turbine Rotor-Stator Interactions in Generating Mode: Pressure Fluctuation in Distributor Channel*. in *23rd IAHR Symposium*. 2006. Yokohama.

[2] NICOLET, C., RUCHONNET, N., AND AVELLAN, F. *One-Dimensional modeling of Rotor Stator Interaction in Francis Pump-Turbine*. in *23rd IAHR Symposium*. 2006. Yokohama.

[3] AUSONI, P., ET AL., *Cavitation influence on von Karman Vortex shedding and induced hydrofoil vibrations.* Journal of Fluids Engineering, 2007. **129**: p. 966-973.

[4] MARSHALL, J. G. AND IMREGUN, M., *A review of aeroelasticity methods with emphasis on turbomachinery applications.* Journal of Fluids and Structures, 1996. **10**(3): p. 237-267.

[5] BRENNEN, F., *A review of added mass and fluid inertial forces*, in *Naval Civil Engineering Laboratory*. 1982.

[6] ABBOTT, I. H., VON DOENHOFF, A. E., AND ALBERT, E., *Summary of Airfoil Data*, in *NACA Report 284*. 1945.

[7] AVELLAN, F., HENRY, P., AND RYHMING, I. L., *A new high speed cavitation tunnel*, in *ASME Winter Annual Meeting*. 1987: Boston.

[8] CARON, J. F., *Etude de l'influence des instationnarités des écoulements sur le développement de la cavitation.*, in *LMH*. 2000, EPFL: Lausanne.

[9] MENTER, F. R., *Two-equation eddy-viscosity turbulence models for engineering application.* AIAA-journal, 1994. **32**(8): p. 1598-1605

[10] KOOCHESFAHANI, M. M., *Vortical patterns in the wake of an oscillating airfoil.* AIAA-journal, 1989. **27**: p. 1200-1205.